Supplementary Information (SI) for Journal of Materials Chemistry A.

Electronic Supplementary Information

Enhancing operational stability and radiation hardness of p-i-n perovskite solar cells *via* a hybrid polymer-based self-assembled hole-transport layer

Victoria V. Ozerova,[a] Olga A. Kraevaya,[a] Nikita A. Emelianov,[a] Tatiana N. Khokhlova,[a] Yuri S. Fedotov,[a,b] Ivan S. Zhidkov,[c,d] Nikita A. Slesarenko,[a] Dmitry P. Kiryukhin,[a] Sergey M. Aldoshin[a], and Pavel A. Troshin*[e,a]

[a] *Federal Research Center of Problems of Chemical Physics and Medicinal Chemistry, Russian Academy of Sciences (FRC PCP MC RAS), Semenov prospect 1, 141432 Chernogolovka, Moscow Region, Russian Federation*

[b] *Institute of Solid State Physics, Russian Academy of Sciences, Academician Osipyan Str. 2, Chernogolovka, 142432, Russia*

[c] *Institute of Physics and Technology, Ural Federal University, Mira 19 Street, 620002 Yekaterinburg, Russia*

[d] *M.N. Mikheev Institute of Metal Physics, Ural Branch of Russian Academy of Sciences, S. Kovalevskoi 18 Street, 620108 Yekaterinburg, Russia*

[e] *Zhengzhou Research Institute of HIT, 26 Longyuan East 7th, Jinshui District, Zhengzhou, Henan Province, 450000, China*

Table of contents

1. Materials

Lead iodide (PbI_2, 99.9985%) and cesium iodide (CsI, 99.999%) were purchased from Lanhit Ltd. and Macklin, respectively. Formamidinium iodide (FAI, 99%), methylammonium chloride (MACl, 99%), phenethylammonium chloride (PEACl, 99%), phenethylammonium iodide (PEAI, 99%), [6,6]-phenyl-C_{61}-butyric acid methyl ester (PCBM, 99%), and 1,3,5-Tris(4-carboxyphenyl)benzene (PTA, 99%) were obtained from FOMaterials, LTD (Russia). Nickel oxide (NiO_x, 99.999%), [4-(3,6-dimethyl-9H-carbazol-9-yl)butyl]phosphonic acid (Me-4PACz, 99%), and 2,9-dimethyl-4,7-diphenyl-1,10-phenanthroline (BCP, 99.5%) were supplied by Advanced Election Technology Co., Ltd. ITO-coated glass substrates (15 Ω sq^{-1}) were obtained from Kintec, while flexible PET/ITO and PEN/ITO substrates were sourced from Advanced Election Technology Co., Ltd. The solvents used included ethanol (EtOH, anhydrous, 99.5%, Macklin), isopropyl alcohol (IPA, high purity, Ekos-1), dimethylformamide (DMF, non-aqueous, 99.8%, Acros Organics), dimethyl sulfoxide (DMSO, non-aqueous, 99.9+%, Sigma-Aldrich), chlorobenzene (CB, 99+%, Acros Organics), and chloroform-d ($CDCl_3$, 99.8%, ABRU258185). The ITO glass cleaning agent (RM11-07) was used as received.

2. Fabrication of solar cells based on 2-step perovskite

The ITO-coated glass substrates were ultrasonically cleaned in a series of solvents: a detergent solution, distilled water, ethanol, and isopropyl alcohol, for 15 minutes each, followed by drying with a nitrogen stream. Subsequently, the pre-cleaned substrates underwent UV-ozone treatment for 50 minutes to remove any residual organic contaminants. A NiOx nanoparticle solution (10 mg/mL in distilled water) was filtered through a 0.45 μm PES syringe filter and then spin-coated onto the ITO/glass at 2000 rpm (1000 rpm/s) for 30 s and annealed at 125°C for 15 minutes in ambient air (52% RH). The samples were then quickly transferred to a glovebox for a second annealing step at 100°C for 10 minutes.

Next, solutions of Me-4PACz, **PTA-COOH**, and Me-4PACz+**PTA-COOH** were prepared and filtered through 0.45 μm PTFE syringe filters prior to spin-coating on rigid substrates using a volume of 100 μL. In all cases, a 10-second delay was incorporated before initiating the spin-coating to ensure sufficient time for molecular binding to the nickel oxide. The Me-4PACz solution (0.3 mg/mL in ethanol) was spun at 4000 rpm, the **PTA-COOH** saturated solution (<0.07 mg/mL in IPA) at 6000 rpm, and the mixed solution (0.3 mg/mL Me-4PACz in saturated **PTA-COOH**/IPA solution) at 2000 rpm (1000 rpm/s acceleration for all), each for 30 s, followed by annealing at 100°C for 10 minutes. The inorganic perovskite precursor solution was prepared by dissolving 1.5 mmol of PbI_2 and 0.075 mmol of CsI in 1 mL of a DMF:DMSO mixture (9:1 v/v) and filtered through a 0.22 μm PTFE syringe filter. This solution (65 μL) was spin-coated onto the HTL at 2500 rpm (1750 rpm/s) for 30 s and then annealed at 70°C for 1 minute Following this, a solution of FAI/MACl (90:12 mg in 1 mL of IPA) was filtered through a 0.22 µm PTFE syringe filter and dynamically spin-coated onto the inorganic layer. The spin-coating program was initiated, and 60 µL of this solution was dispensed 5 seconds after the process start, followed by spinning at 2750 rpm for 35 s (glovebox temperature maintained at 21.4–21.7°C). The resulting film was annealed at 100°C for 30 minutes inside the N_2 glovebox.

For post-treatment, a PEACl solution (1.5 mg/mL in an IPA:DMSO mixture, 150:1 v/v) was filtered through a 0.45 µm PTFE syringe filter and dynamically spin-coated onto the perovskite surface using a volume of 65 µL at 2000 rpm for 30 s and annealed at 100°C for 10 minutes. Thereafter, a $PC_{61}BM$ solution (20 mg/mL in $CDCl_3$) was filtered through a 0.45 µm PTFE syringe filter, and a 35 µL aliquot was dynamically deposited and spin-coated at 4000 rpm for 30 s; this deposition and spin-coating process was repeated once before a final anneal at 100°C for 5 minutes. Next, the BCP layer was deposited by spin-coating 100 µL of its solution (0.5 mg/mL in IPA), filtered through a 0.45 µm PTFE syringe filter, at 4000 rpm (1000 rpm/s) for 30 s. Finally, a 120 nm-thick Ag top electrode was thermally evaporated at a rate of 1-2 Å/s through a shadow mask under a vacuum of 9×10^{-6} mbar, defining an active device area of 0.21 cm^2.

3. Fabrication of solar cells for MPPT stability tests

Solar cells for the MPPT stability tests were fabricated identically in all layers except for the perovskite composition and the top electrode. The $Cs_{0.05}FA_{0.95}PbI_3$ perovskite layer was deposited following the method reported by Gong et al.[1] Specifically, the Ag electrode was replaced with a 120 nm-thick Al layer, thermally evaporated at a rate of 2–4 Å/s.

4. Fabrication of flexible solar cells for gamma rays stability tests

The devices for gamma rays stability testing were fabricated following the same procedure as described in Section 2, with three key modifications: (1) the rigid glass/ITO substrates were replaced with flexible PET/ITO or PEN/ITO substrates, which, instead of solvent cleaning, were treated with air plasma for 30 minutes; (2) the perovskite active layer consisted of $Cs_{0.05}FA_{0.95}PbI_3$, deposited according to the method outlined in Section 3; and (3) the active area of these flexible devices was defined as 0.06 cm^2. To ensure flatness and mechanical stability during the deposition of all subsequent layers, the flexible substrates were temporarily bonded to a rigid glass carrier using a 200 µm thick layer of polydimethylsiloxane (PDMS). Prior to the current density-voltage (J-V) characterization, the PDMS layer was removed to delaminate the finished flexible devices from the glass carrier.

5. Thermal cycling stability test protocol

The unencapsulated devices were sealed in airtight polymer envelopes inside a nitrogen-filled glove box prior to being subjected to thermal cycling, ensuring an inert atmosphere throughout the test. The thermal cycling program consisted of repeated 152-minute cycles: heating from 28.8°C to +80°C over 6 min (30 min dwell), cooling to -85°C over 78 min (30 min dwell), and returning to 28.8°C over 8 min. Thermal cycling was performed using an EVCLIM-KTX-80-D1 Z chamber (ERSTVAK Ltd).

6. Characterization

Cyclic voltammetry (CV) measurements for the polymer films were performed using an Elins P-30SM potentiostat at room temperature with a potential sweep rate of 50 mV s^{-1}. UV-vis absorption spectra were recorded using an Avantes AvaSpec-2048 optical fiber spectrometer. Nuclear magnetic resonance (NMR) spectra were collected using a Bruker 500MHz FT-NMR instrument spectrometer (Bruker, AVANCE III). The molecular weight characteristics of polymer P1 were determined by gel permeation chromatography (GPC) using a Shimadzu high-performance liquid chromatography system equipped with an SPD-20A spectrophotometric detector. The contact angles were measured using a DSA25S Kruss drop-shape analyzer. The IR s-SNOM measurements were performed using a neaSNOM microscope (Neaspec, Haar, Germany) in PsHet mode with a Mid-IR laser MIRcat-2400 (Daylight Solutions, USA) installed inside the MBraun glove box (O_2 < 0.1 ppm, H_2O < 0.1 ppm). Steady-state PL spectra were measured under a nitrogen atmosphere inside a glove box using Ocean Insight QE Pro spectrometer and a 450 nm laser as the excitation source. The device characterization was performed inside an MBraun glovebox under a nitrogen atmosphere using simulated AM 1.5G irradiation (LSS-100, China) at 100 mW cm^{-2} using Advantest R6240A source-measurement units. The light flux was calibrated using a silicon diode with a known spectral responce. The EQE measurements were performed under ambient conditions for nonencapsulated devices. The EQE setup included 300 W Xenon lamp as a light source and automatic monochromator from LOMO instruments, Russia. The signal detection and processing were performed using SR510 lock-in amplifier combined with SR540 optical chopper (both from Stanford Research Instruments, USA). The MPPT stability tests were performed inside the MBraun glove box (O_2 < 0.1 ppm, H_2O < 0.1 ppm) using HONG PEI S&T CO., LTD test system (Shanghai, China). The IS and Mott-Schottky measurements were performed using PS-20 instrument. The time-of-flight secondary ion mass spectrometry (ToF-SIMS) chemical mapping was performed using a TOF.SIMS 5-100P instrument (ION-TOF GmbH, Germany). The mapping was carried out separately for positive and negative ions due to the technique limitations. Prior to the analysis, the sample surface was cleaned over an area of 1000 × 1000 μm^2 using a 2 keV ion beam with an exposure time of 30 s. The sputter beam was 340 nA O_2^- or 120 nA Cs^+ for the negative and positive secondary ion analysis, respectively. The ion analysis consisted of Bi^+ pulses (25 keV ion energy, 20 ns pulse duration, 3.5 pA measured sample current) and was set in spectroscopy (high-current bunched) mode with an effective target pulse width of ~1 ns. For all the interest fragments, the mass resolution was >7000 (m/δm). After data collection, the total area images were individually reconstructed and analysed. The colour scales of the reconstructed ion images were set equally between the samples separately for each species to allow a fair comparison of the secondary ion intensity.

7. Additional Discussion on the Synthesis and Molecular Weight Distribution of ***PTA-COOH***

We believe that the broad molecular weight distribution does not critically affect the poly-SAM performance, as the multisite anchoring of multiple carboxylic groups along each polymer chain ensures robust surface binding and uniform coverage regardless of chain length variations. Thus, the key advantages of the poly-SAM approach are preserved. Nevertheless, polymer parameters such as molecular weight (Mw) and polydispersity index (PDI) influence the solubility, film formation, rheological properties, and carrier mobility.[2] As noted in the main text, polymer PTA-COOH was synthesized via oxidative polymerization using $FeCl_3$, the high PDI was obtained due to the chosen method of oxidative polymerization.

Although oxidative polymerization is rarely considered as a suitable method for PSCs materials synthesis, this approach is very simple and affordable. Particularly, in our previous work we have demonstrated that HTL based on polytriarylamines, synthesized by oxidative polymerization, allowed to fabricate PSCs with PCEs higher than those of PSCs fabricated using commercial PTAA, obtained from Osilla.[3]

Some reports have discussed optimization of the molecular weights and PDIs of polyarylamines. For example, Di Carlo et al. have varied the molecular weight of doped poly(triarylamine) HTM, which allowed to improve by one order of magnitude the charge mobility inside the HTL and the charge transfer at the perovskite/HTL interface. Particularly, slower charge recombination was shown for the devices with high-Mw PTAA.[4]

Jun and colleagues studied a series of PTAs with different molecular weights (Mw) and polydispersity indices. The lowest Mw polymer film (10 kDa) displayed nonuniformity, likely because it has a short chain length that cannot effectively bridge the lithium dopant-coordinated domains. For the 40 kDa high-PDI value polymer-based film, morphology similar to that of the low-Mw polymer films was shown.[5]

Since the impact of varying molecular weight and polydispersity index in standard HTLs and SAMs is system-dependent, these parameters should ideally be optimized for each specific system.

Several strategies have been reported to improve polymer uniformity and achieve narrower PDIs, presenting a potential direction for future work. First, optimization of the oxidative polymerization conditions (adjusting the monomer-to-oxidant ratio and varying reaction temperature) might lead to lower PDIs. For example, Siove et al. have demonstrated that lower amounts of $FeCl_3$ equivalents to monomer reduce PDI and Mw values of the resulting polymer.[6]

Another useful method to change Mw and PDI values could be post-polymerization fractionation. Employing Soxhlet extraction with sequential solvents could allow isolating only the mid-to-high molecular weight fraction of PTA-COOH. Future studies might also explore direct arylation polymerization (DArP) or Suzuki-Miyaura coupling for carboxylic-acid-functionalized PTA, which generally offer superior control over molecular weight and PDI (<1.5) compared to oxidative methods.

8. Figures and tables

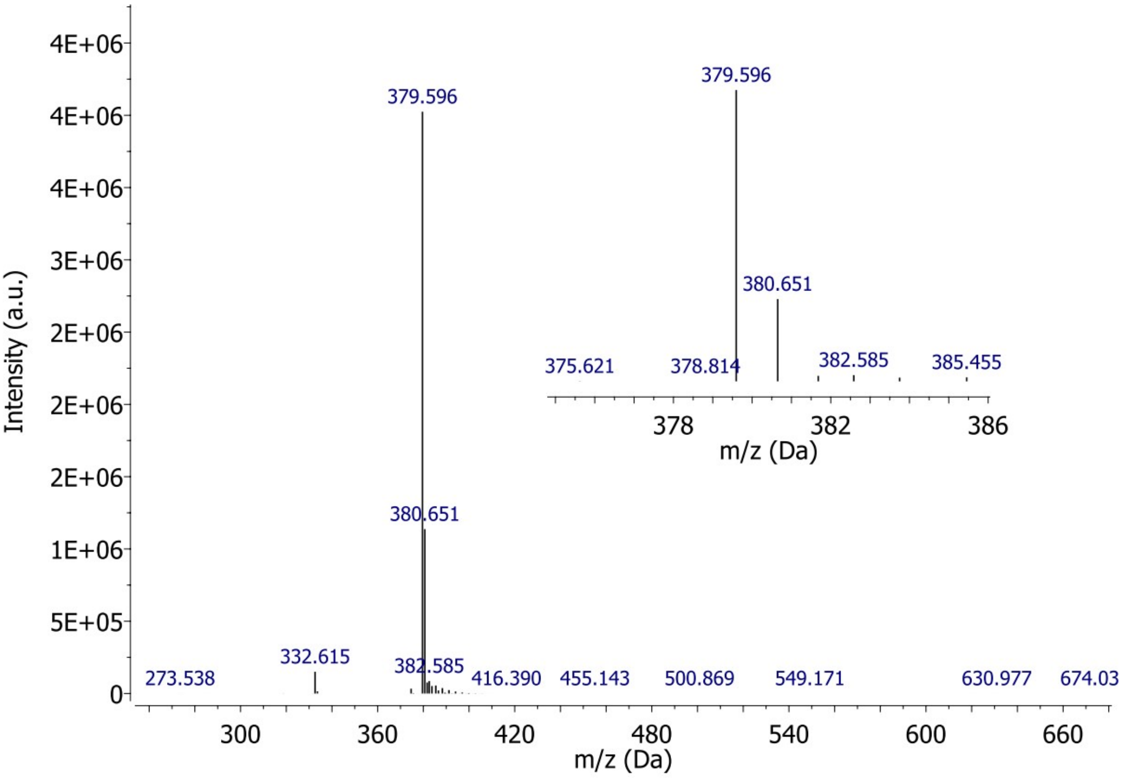

Figure S1. MALDI mass spectrum of compound M1.

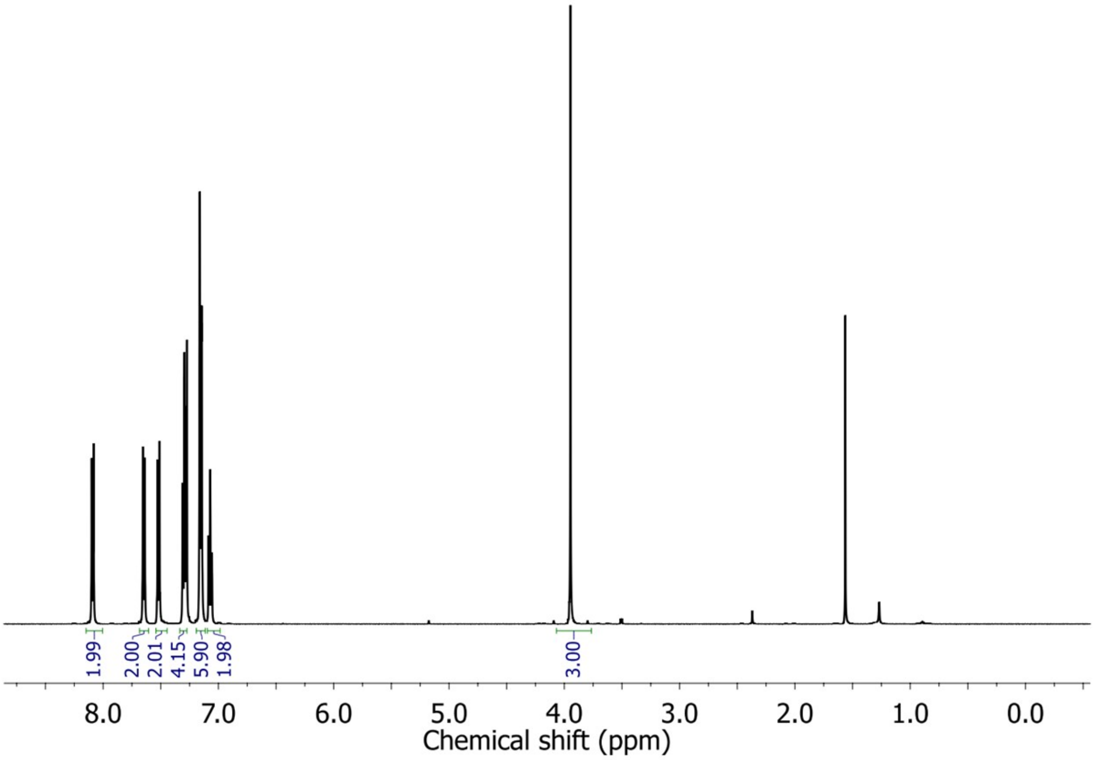

Figure S2. ^{1}H NMR spectrum of compound M1.

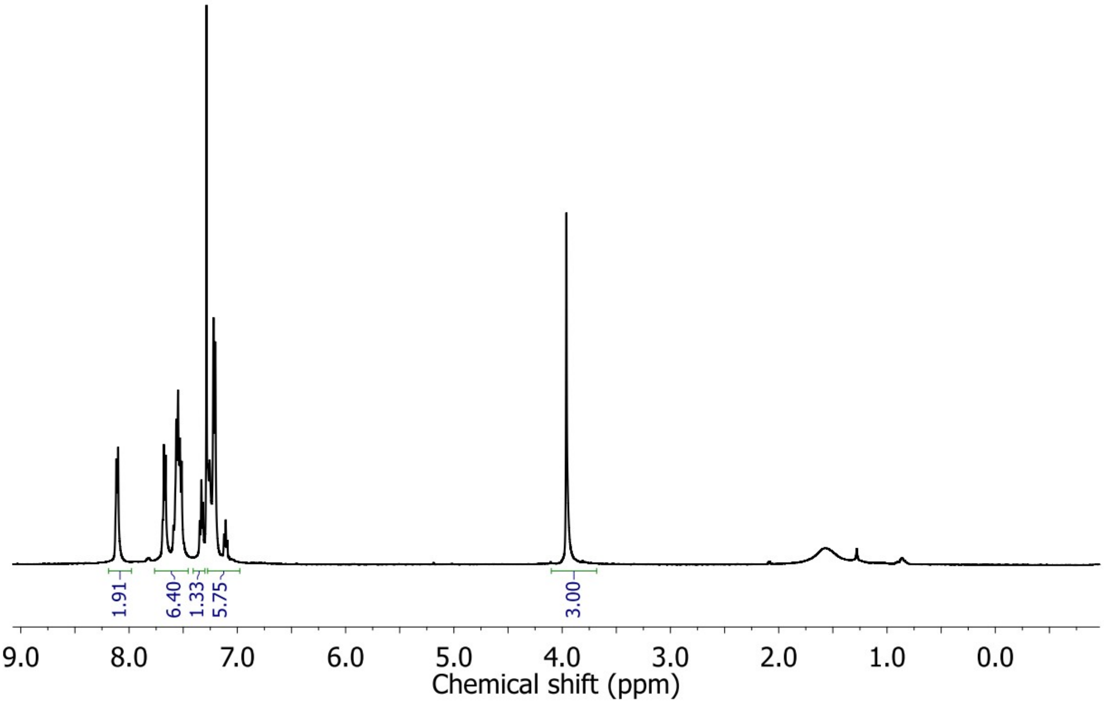

Figure S3. ^{1}H NMR spectrum of P1.

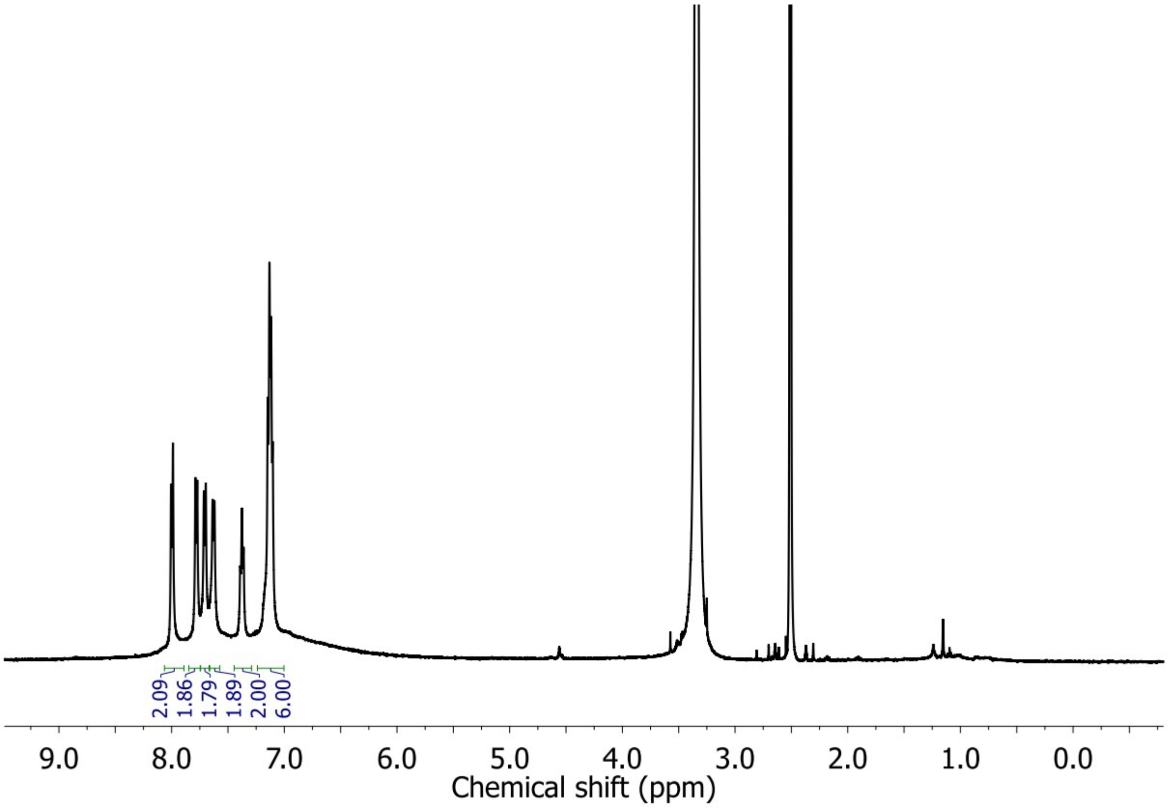

Figure S4. ^{1}H NMR spectrum of compound **PTA-COOH**.

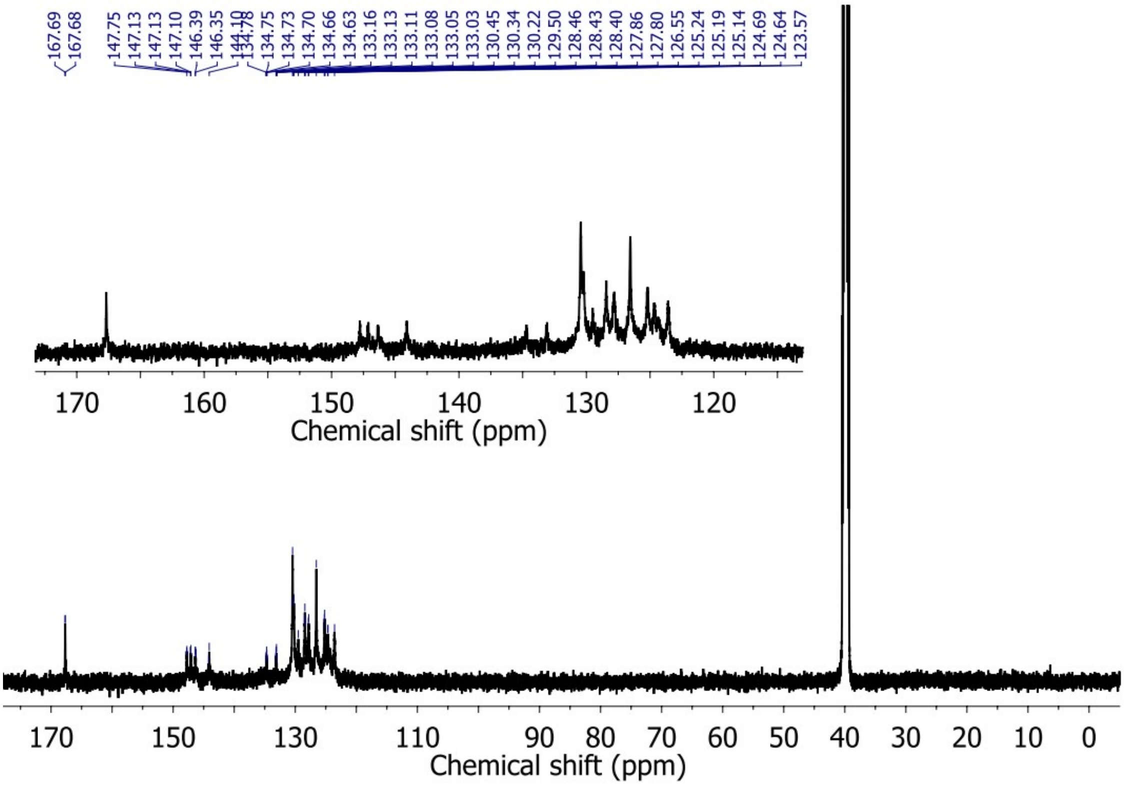

Figure S5. ^{13}C NMR spectrum of compound **PTA-COOH**.

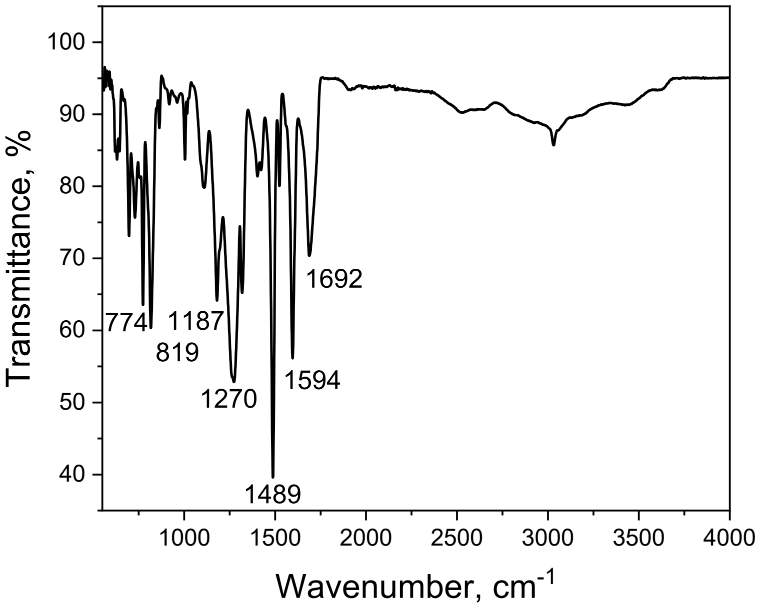

Figure S6. FTIR spectrum of polymer **PTA-COOH**.

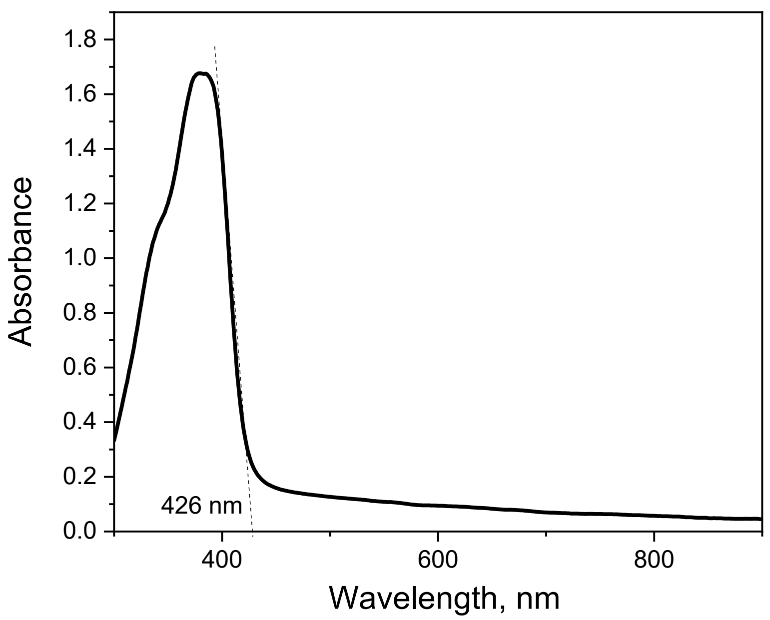

Figure S7. UV-vis absorption spectrum of polymer **PTA-COOH**.

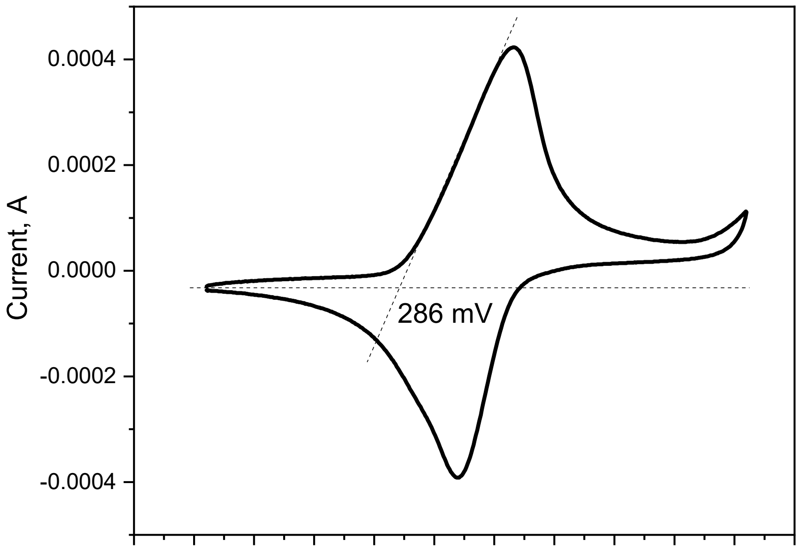

Figure S8. Cyclic voltammetry for polymer **PTA-COOH**.

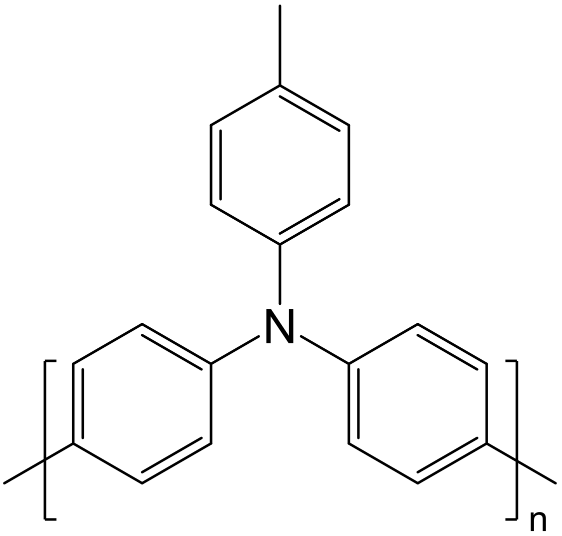

Figure S9. **PTA** (Poly[bis(4-phenyl)(4-methylphenyl)amine] molecular structure[7]

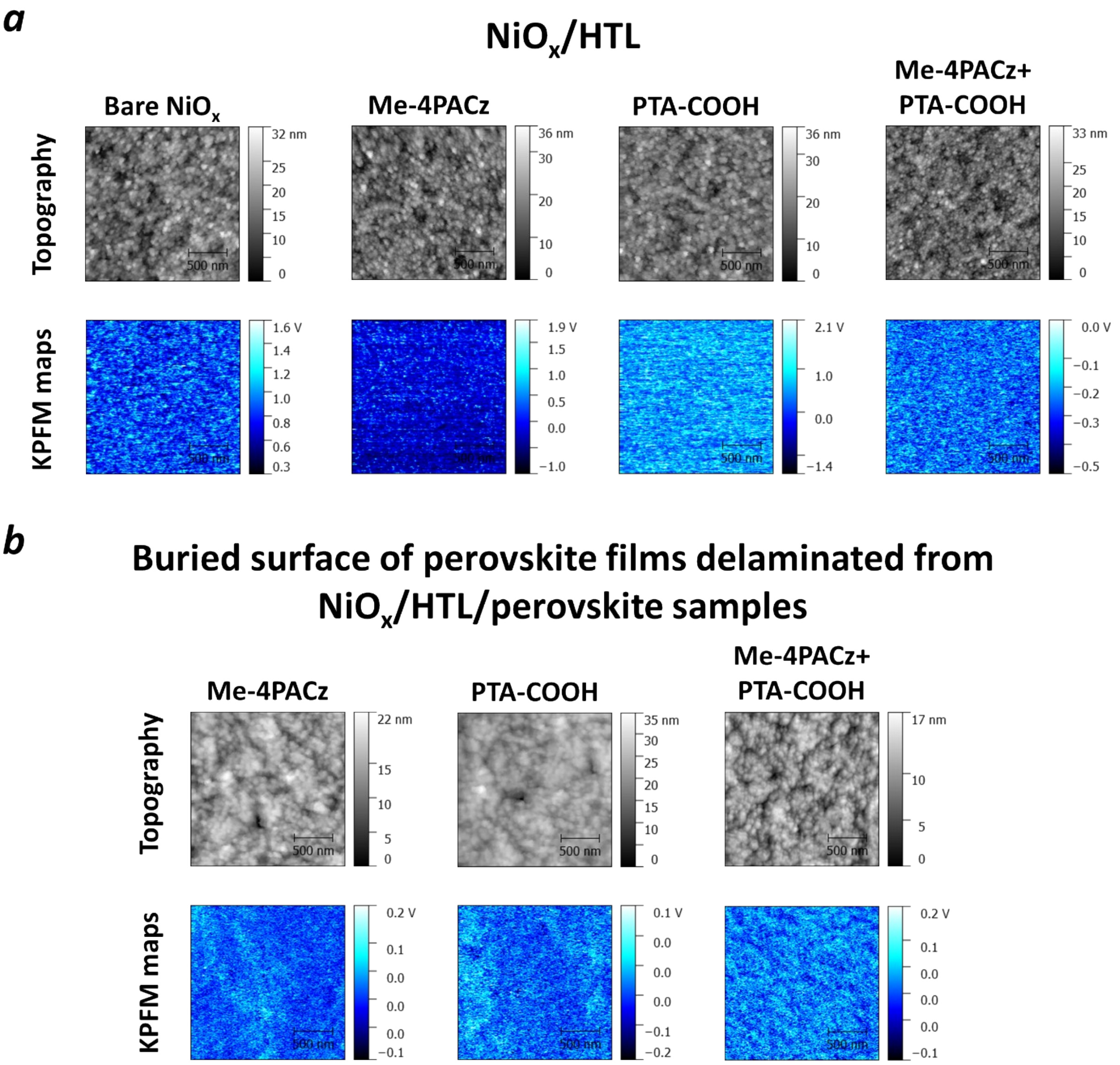

Figure S10. Film topography and KPFM mapping data. (a) Bare NiO_x and HTL interlayers deposited on NiO_x: Me-4PACz, **PTA-COOH** and Me-4PACz+**PTA-COOH** blend. (b) Buried interfaces prepared by delamination of the perovskite films from the ITO/NiO_x/HTL/perovskite samples, where HTL is represented by Me-4PACz (left), **PTA-COOH** (middle) and Me-4PACz+ **PTA-COOH** (right).

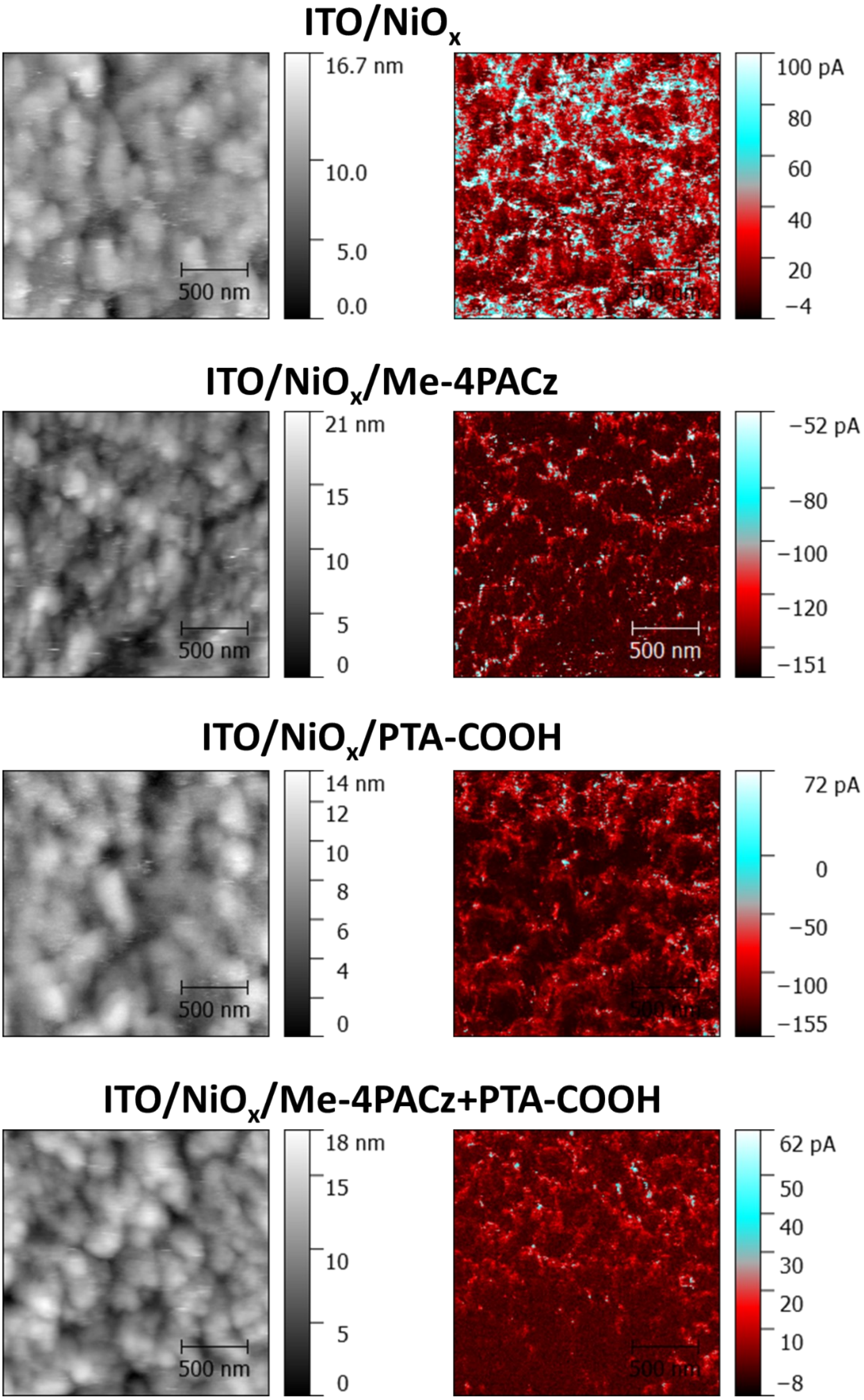

Figure S11. Film topography and c-AFM mapping data. (a) Bare NiO$_x$ and HTL interlayers deposited on NiO$_x$: Me-4PACz, **PTA-COOH** and Me-4PACz+**PTA-COOH** blend.

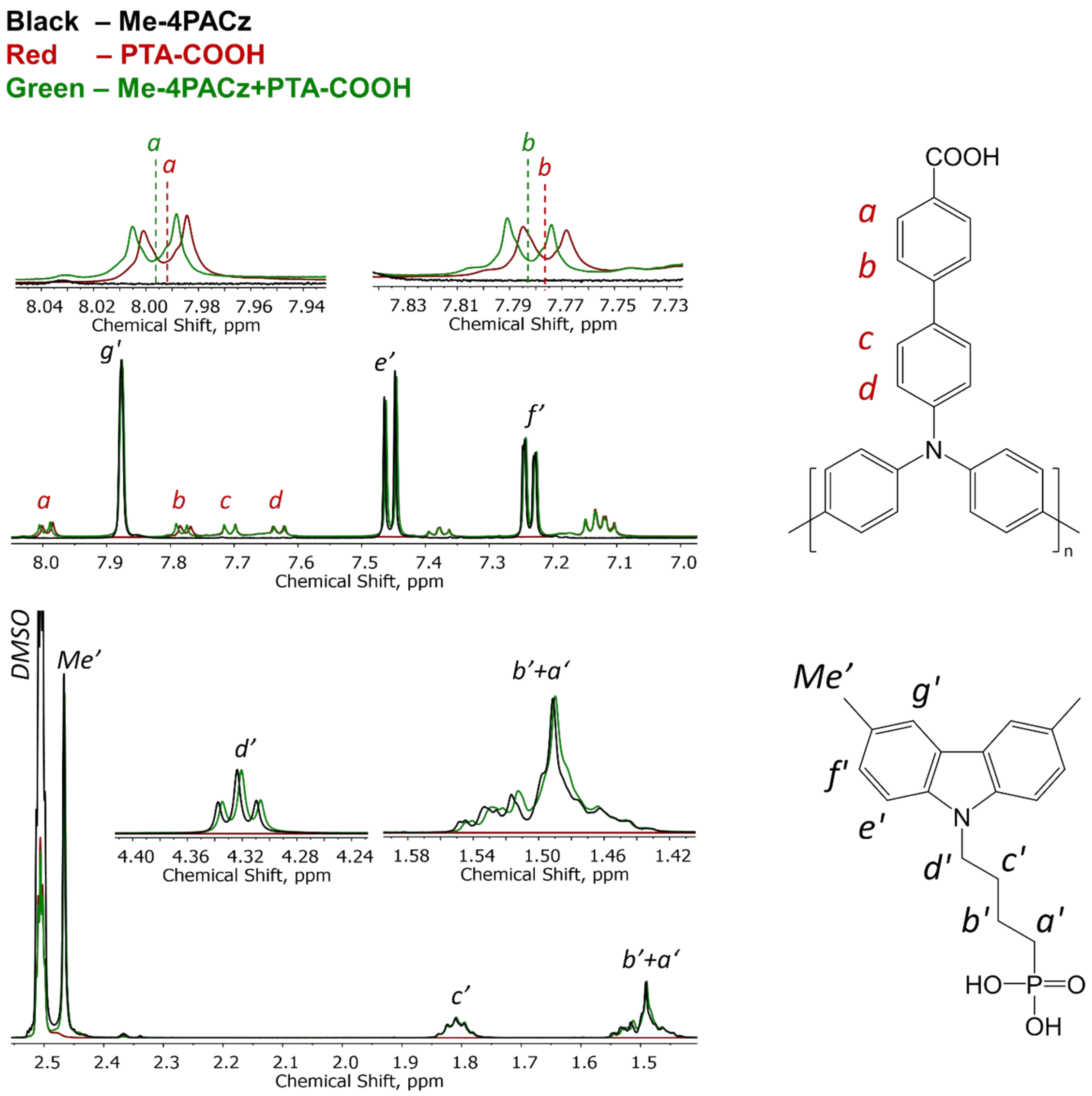

Figure S12. ^{1}H NMR spectra comparison for Me-4PACz, **PTA-COOH** and Me-4PACz+**PTA-COOH** solutions in DMSO-d$_6$

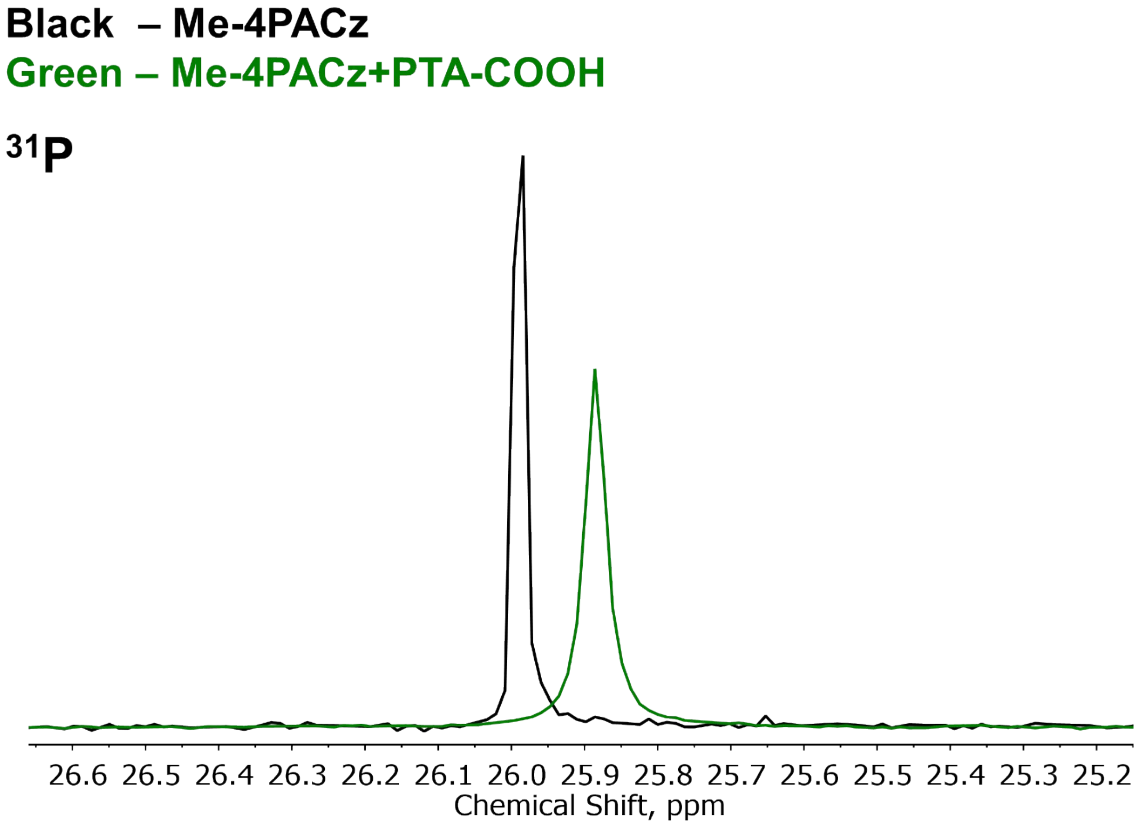

Figure S13. ^{31}P NMR spectra comparison for Me-4PACz and Me-4PACz+**PTA-COOH** solutions in DMSO-d_6

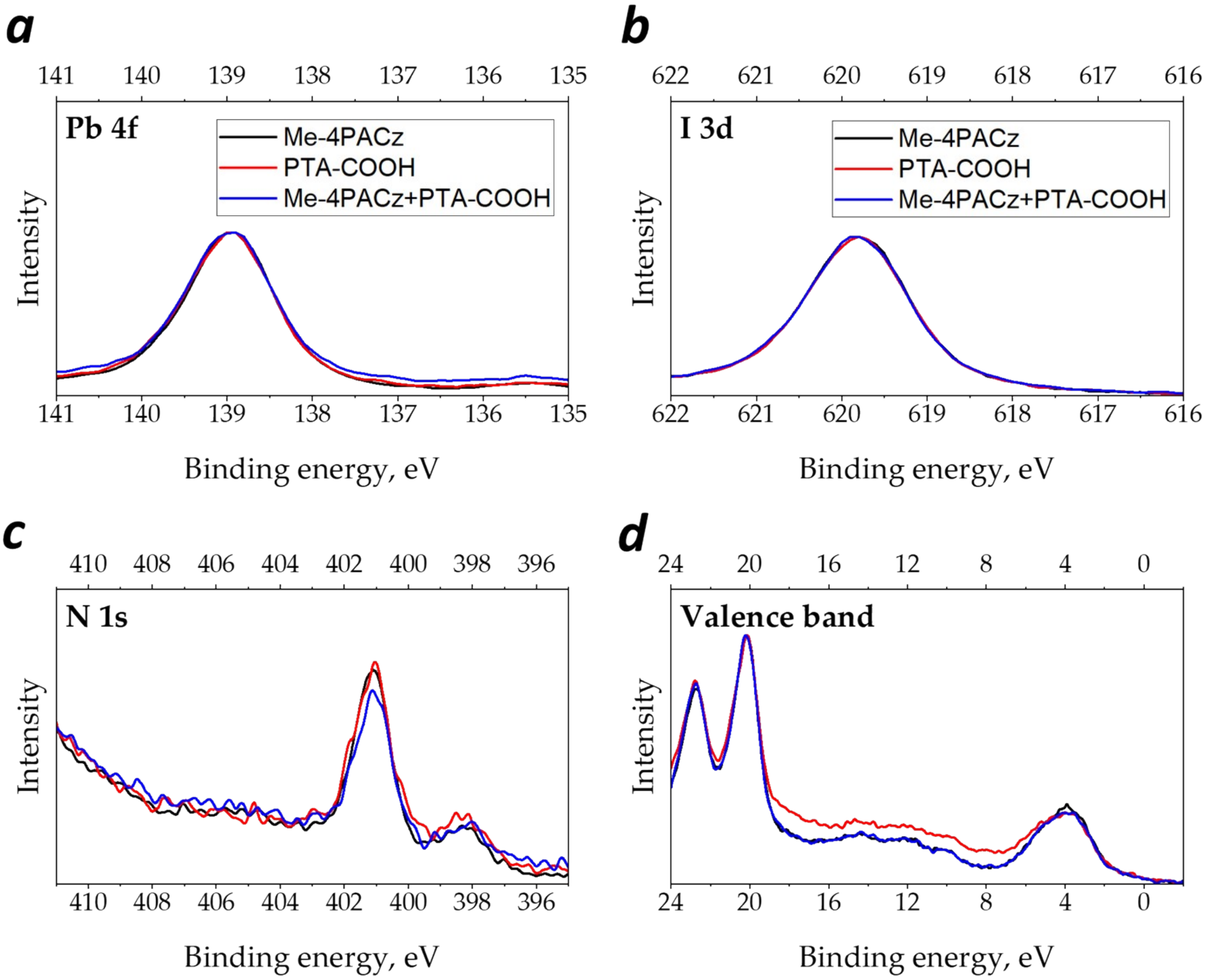

Figure S14. XPS spectra of the perovskite film surface deposited on Me-4PACz (black), **PTA-COOH** (red), and Me-4PACz+**PTA-COOH** (blue): (a) Pb 4f, (b) I 3d, (c) N 1s core levels, and (d) valence band region.

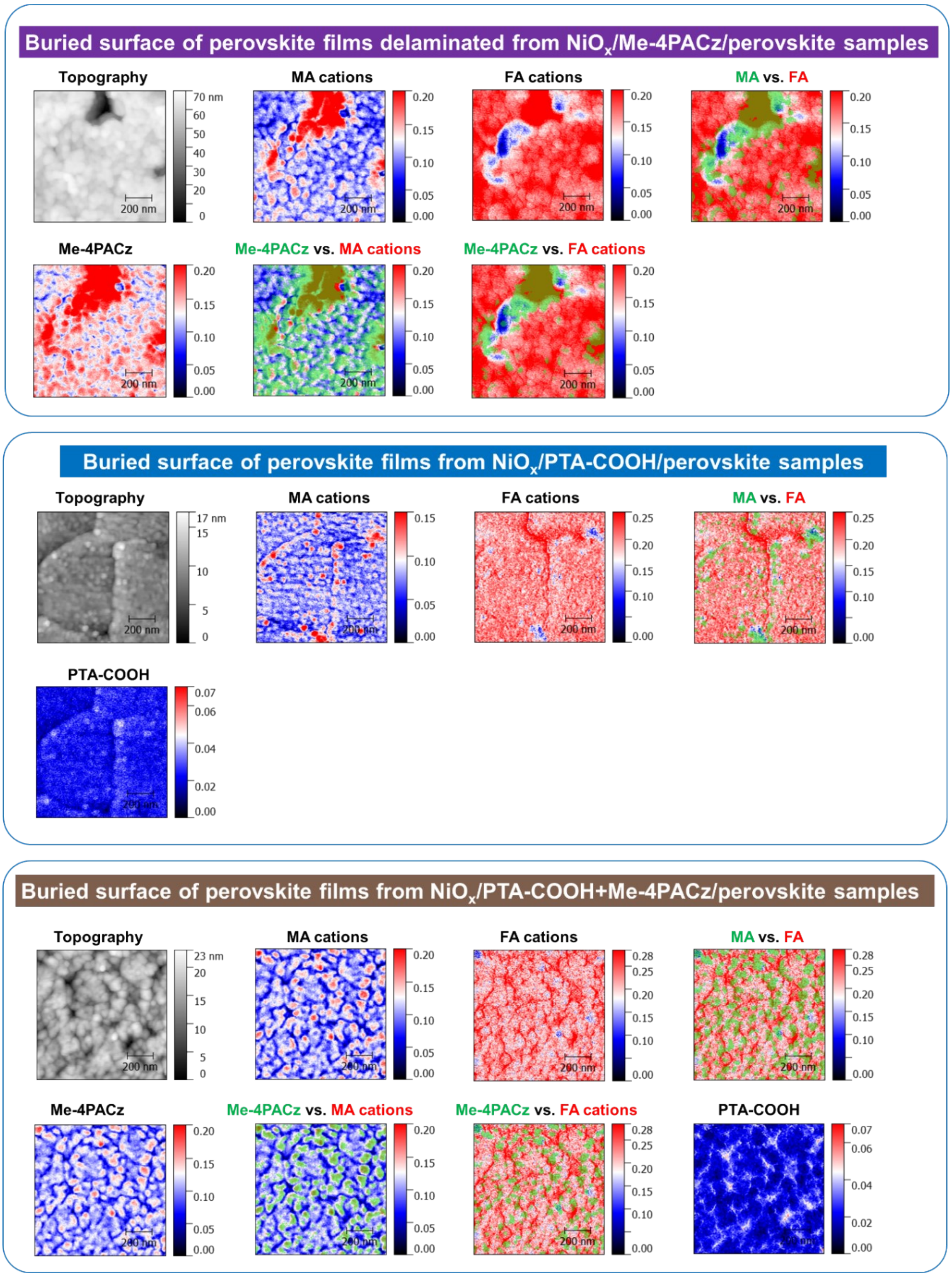

Figure S15. Film topography and IR s-SNOM mapping data for buried interfaces prepared by delamination of the perovskite films from the ITO/HTL/perovskite samples, where HTL is represented by NiO_x/Me-4PACz (top), NiO_x/**PTA-COOH** (middle) and NiO_x/Me-4PACz+**PTA-COOH** (bottom). Caption above the SNOM image indicates the probed component. For the colocalization images, the components marked in green and red colors in the caption are shown in the same colors on the maps. Blue color in all images correlates with the areas with low local concentration of the probed component.

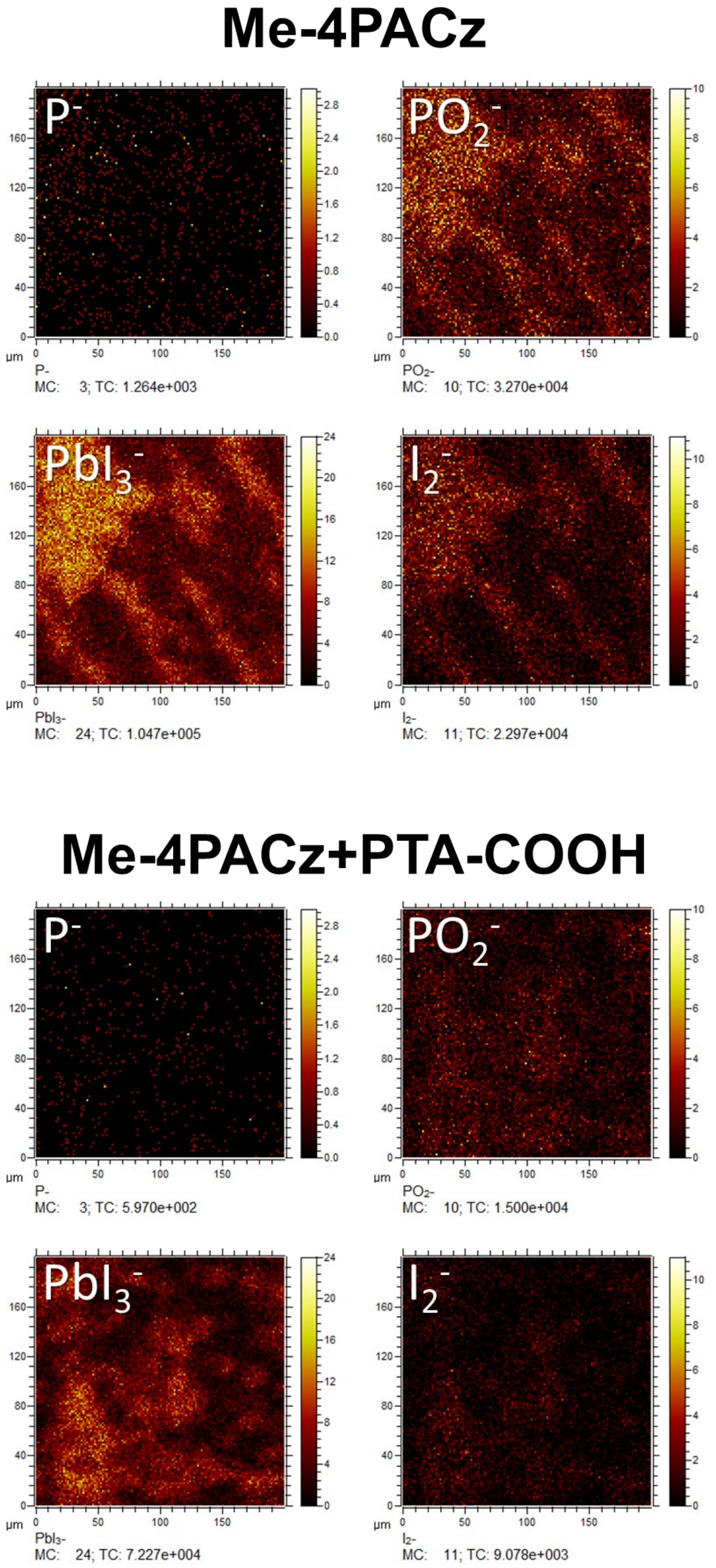

Figure S16. TOF-SIMS maps with 0.2 μm resolution visualizing the distribution of P^-, PO^{2-}, PbI_3^-, I_2^- ions from the buried surface of perovskite films deposited on Me-4PACz and Me-4PACz+**PTA-COOH** layers.

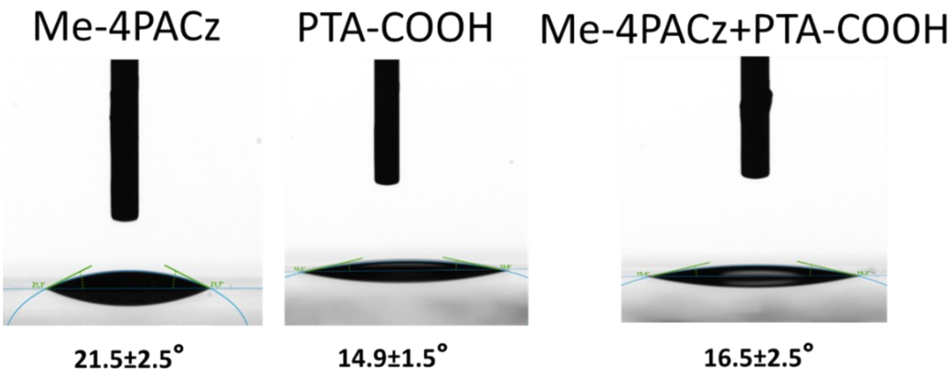

Figure S17. Wetting of different HTL films by the 1.5 M PbI_2 + 0.075 M CsI precursor solution in DMF:DMSO 9:1 (v/v). Average contact angles obtained from the analysis of 5 independent measurements are given under the photographs.

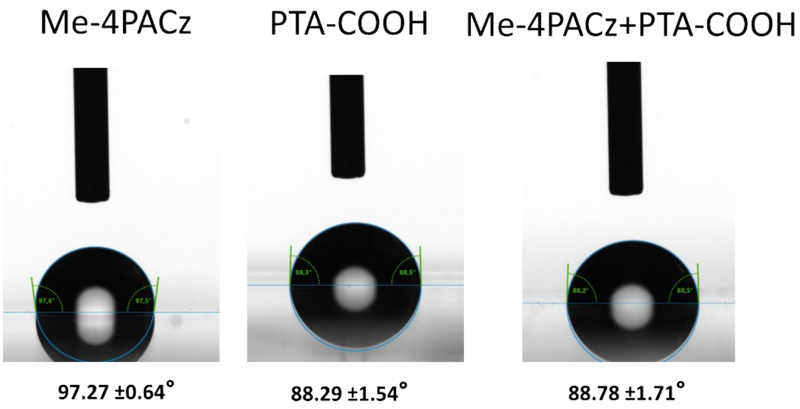

Figure S18. Water contact angles for different HTL films. Average contact angles obtained from the analysis of 5 independent measurements are given under the photographs.

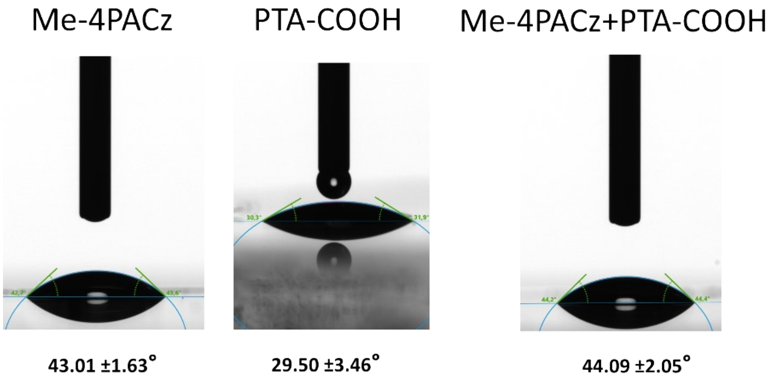

Figure S19. CH_2I_2 contact angles for different HTL films. Average contact angles obtained from the analysis of 5 independent measurements are given under the photographs.

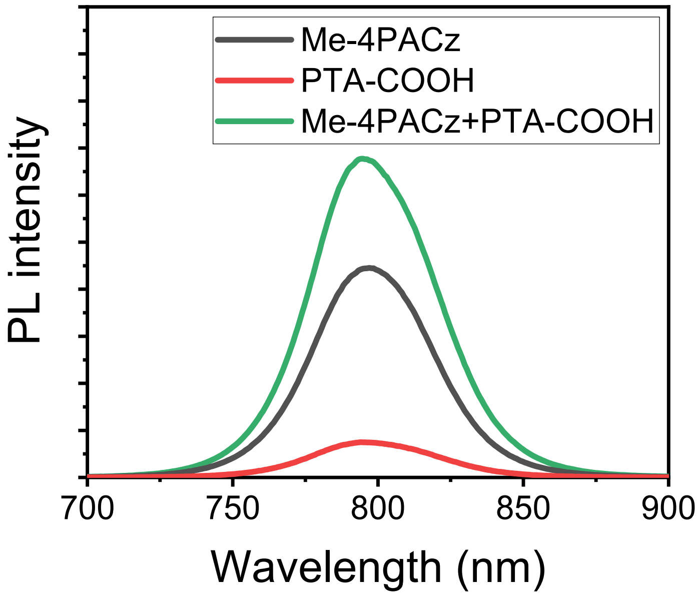

Figure S20. Steady-state PL spectra for different ITO/NiO_x/HTL/perovskite stacks.

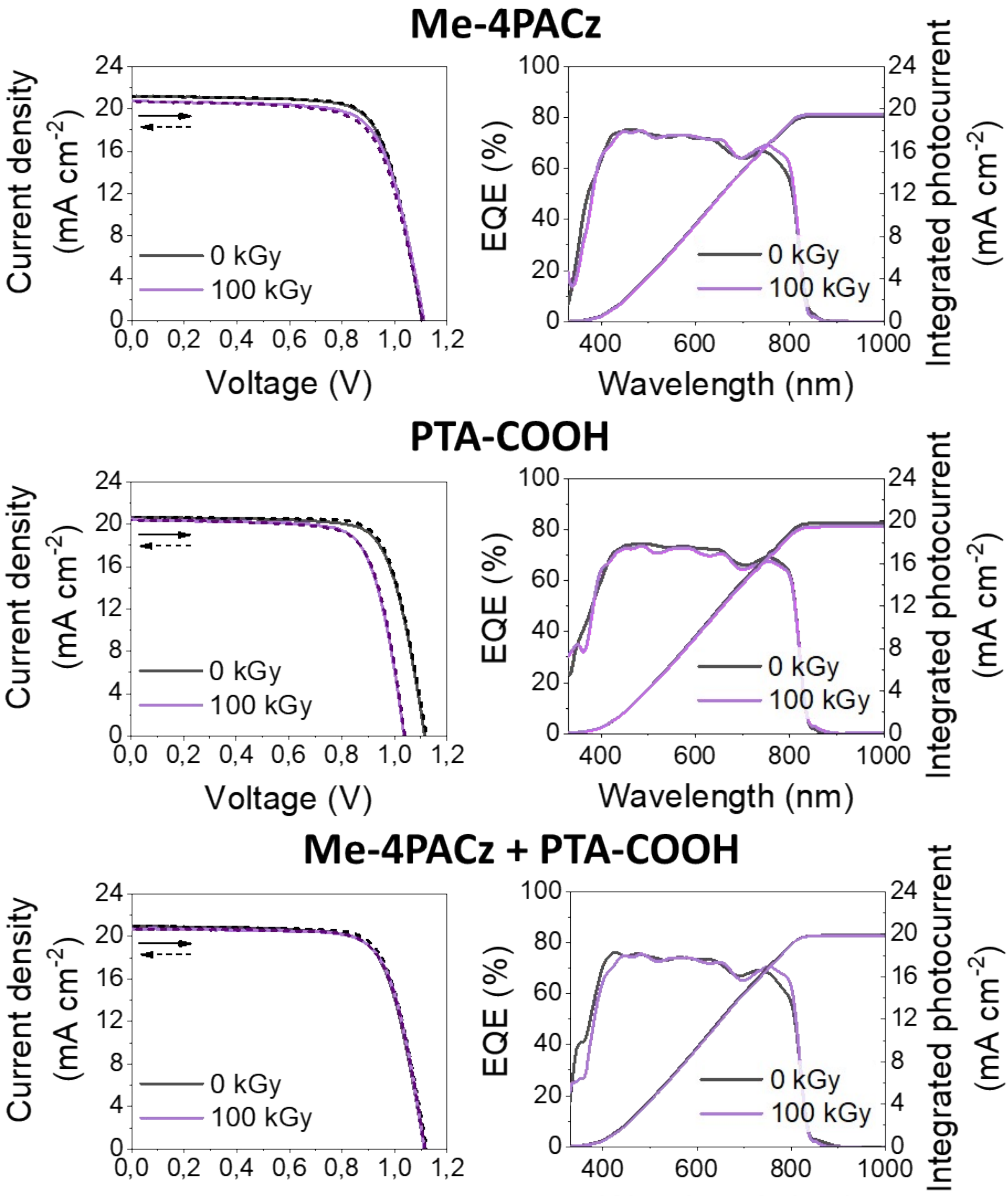

Figure S21. Radiation hardness of flexible PSCs on PET/ITO substrates using different HTLs. The evolution of the J-V characteristics and EQE spectra after exposure of the devices to 100 kGy of gamma rays.

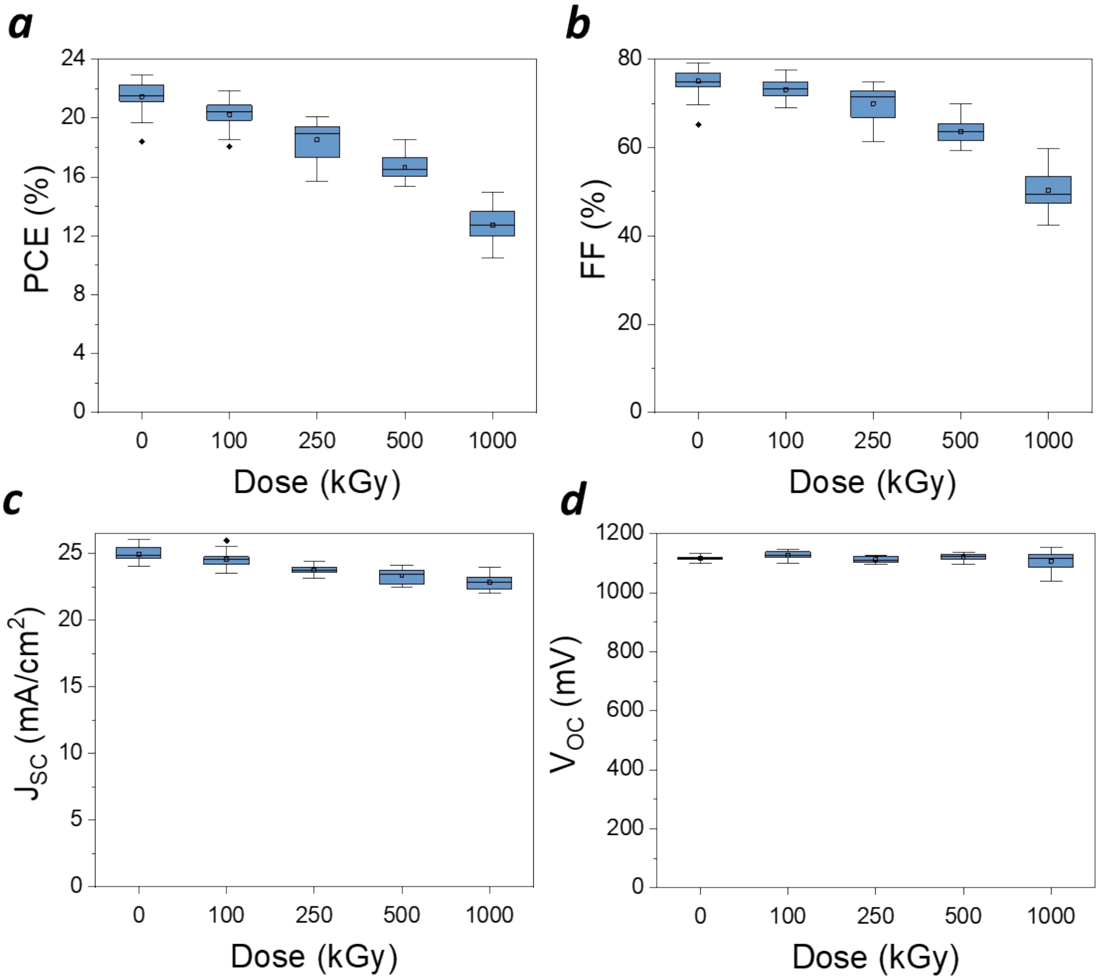

Figure S22. Performance of flexible devices versus accumulated ^{60}Co gamma-ray dose: PCE (a), FF (b), J_{SC} (c), V_{OC} (d). Device structure: PEN/ITO/NiO_x/Me-4PACz+**PTA-COOH**/$Cs_{0.05}FA_{0.95}PbI_3$/PEACl/$PC_{61}BM$/BCP/Ag

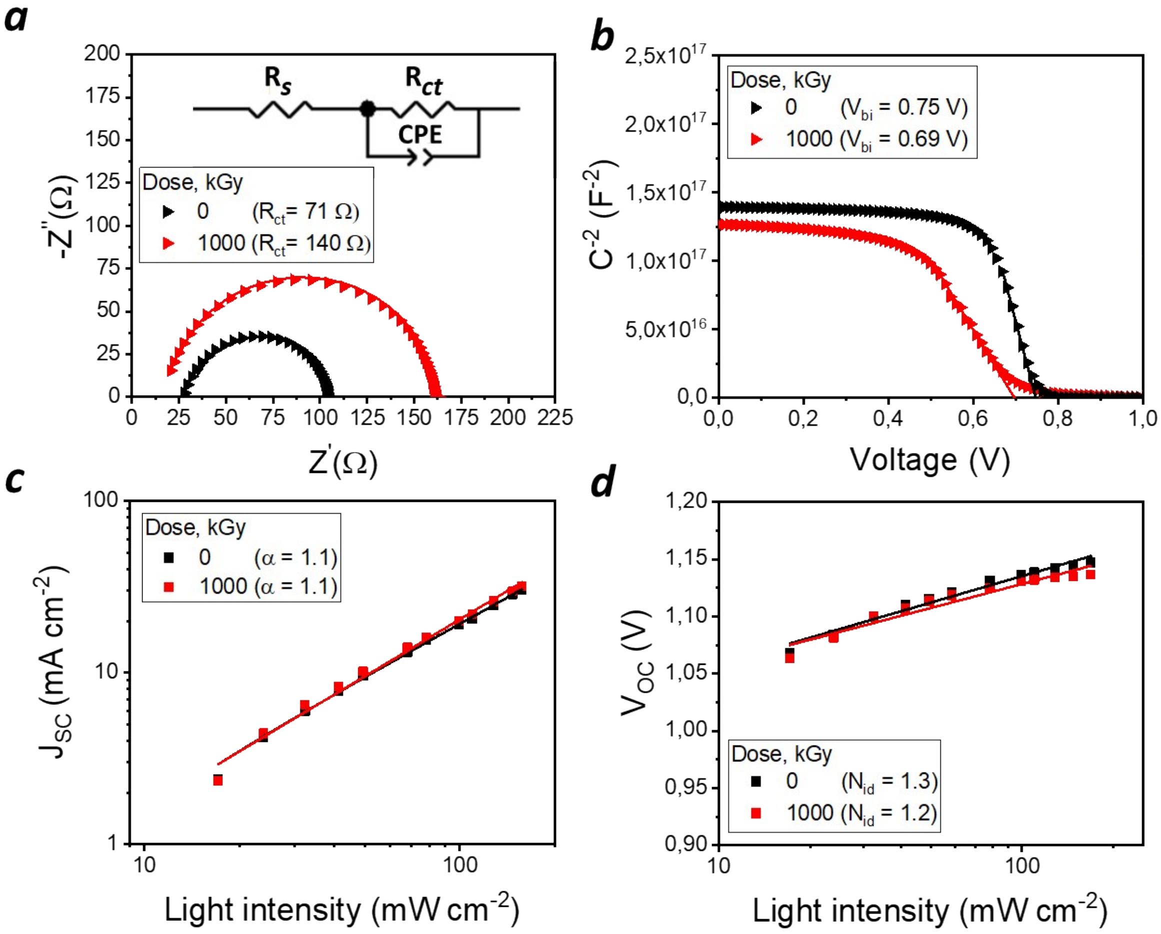

Figure S23. Electrophysical characterization of f-PSCs before (black) and after (red) exposure to 1 MGy dose of ^{60}Co gamma-rays. Nyquist plots (a), capacitance-voltage (C-V) characteristics (b). and light-intensity dependence of the short-circuit current density (J_{SC}) (c) and open-circuit voltage (V_{OC}) (d). Device structure: PEN/ITO/NiO_x/Me-4PACz+**PTA-COOH**/$Cs_{0.05}FA_{0.95}PbI_3$/PEACl/$PC_{61}BM$/BCP/Ag

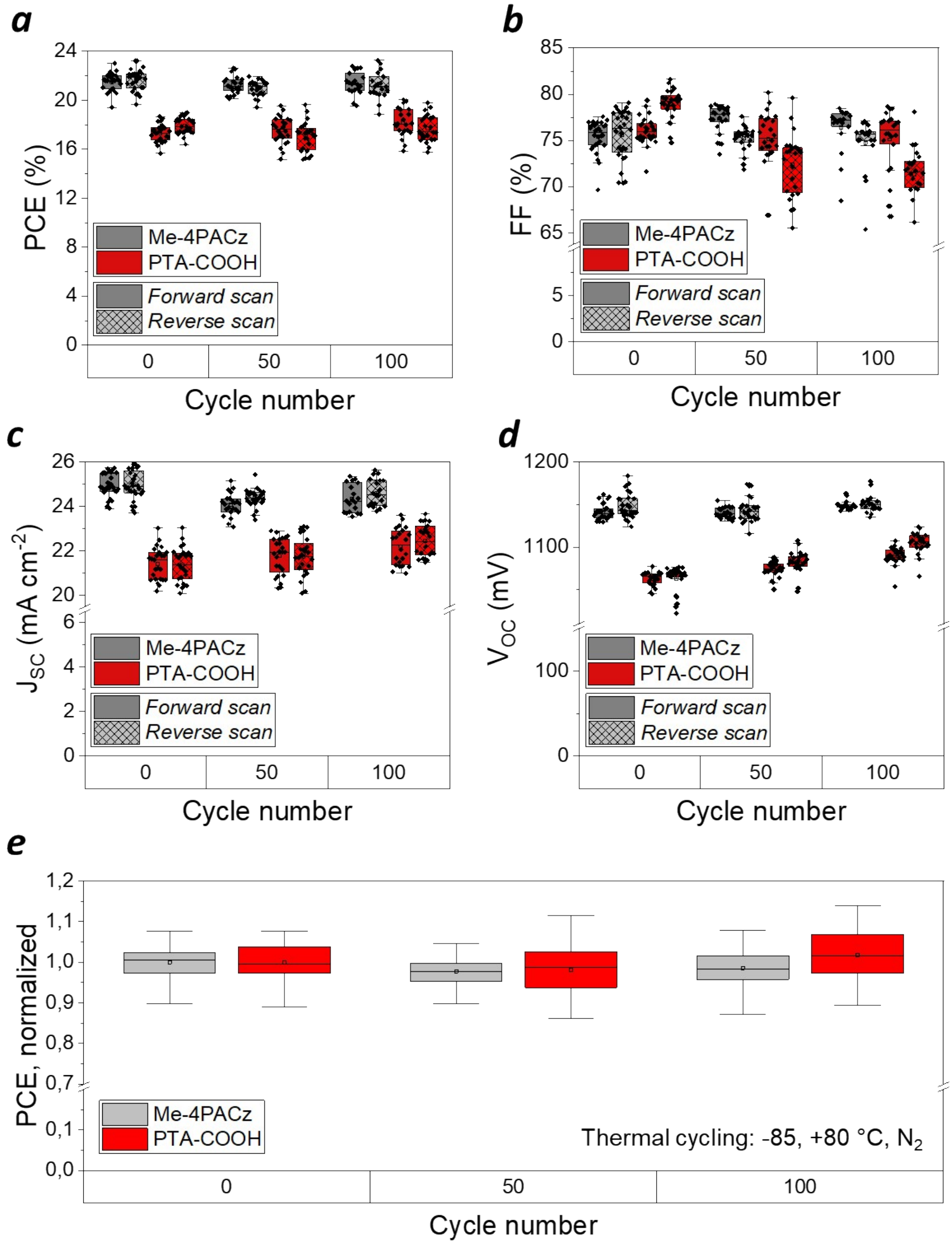

Figure S24. Thermal cycling stability of PSCs based on Me-4PACz and **PTA-COOH** HTLs under extreme temperature stress (-85°C to +80°C, 100 cycles). PCE (a), FF (b), J_{SC} (c), V_{OC} (d). Device structure: glass/ITO/NiO_x/HTL/$Cs_{0.05}FA_{0.95}PbI_3$/PEACl/$PC_{61}BM$/BCP/Ag with an active area of 0.06 cm^2

Table S1. Analysis of the KPFM data for ITO/NiO_x/HTL and ITO/NiO_x/HTL/Perovskite stacks

HTL	**W_F (eV)**	
	HTL surface	Buried interface of the perovskite film deposited on the corresponding HTL
Me-4PACz	-4.93	-4.93
PTA-COOH	-4.70	-4.96
Me-4PACz + PTA-COOH	-4.86	-4.94
Bare NiO_x	-5.73	

Table S2. Analysis of the TRPV data for PSCs fabricated using different HTLs

HTL	TRPV data			
	A_1	t_1, µs	**A_2**	t_2, µs
PTA	0.44	197	0.34	5501
Me-4PACz	0.44	290	0.35	5906
PTA-COOH	0.44	142	0.27	3771
Me-4PACz + PTA-COOH	0.5	373	0.37	3217

t_1 – carrier lifetime

t_2 – characteristic time of ion motion within the perovskite film

Table S3. Characteristics of PSCs using different HTLs extracted from impedance spectroscopy[8] measurements and Mott-Schottky analysis. The impedance spectroscopy measurements were performed in the dark with a bias voltage of -50 mV applied relative to the open-circuit voltage (V_{OC}).

HTL	**R_s, Ω**	**R_1, kΩ**	**R_2, kΩ**	**R_3, kΩ**	**V_{bi}, mV**	**N_{eff}, cm^{-3}**
PTA	10.3	46.5 ± 5.5	83.0 ± 19.0	270.5 ± 11.3	892	$2.93\cdot10^{14}$
Me-4PACz	12.0	85.8 ± 8.1	214.3 ± 8.9	-	963	$4.65\cdot10^{14}$
PTA-COOH	11.3	19.6 ± 3.9	87.2 ± 6.9	133.9 ± 8.8	896	$2.24\cdot10^{14}$
Me-4PACz + PTA-COOH	11.7	62.9 ± 4.7	238.1 ± 5.4	-	1006	$5.27\cdot10^{14}$

R_1 – charge transfer resistance, R_2 – recombination resistance, R_3 – ionic transport resistance.

Table S4. Surface properties of different ITO/NiO_x/HTLs stacks

HTL	Surface free energy, mN/m	Disperse component, mN/m	Polar component, mN/m	Contact angles, °		
				water	CH_2I_2	PbI_2 + CsI solution
Me-4PACz	45.22±1.68	44.43±1.41	0.80±0.27	97.27 ±0.64	43.01 ±1.63	21.5±2.5
PTA-COOH	38.24±0.91	38.07±0.85	0.18±0.06	88.29 ±1.54	29.50 ±3.46	14.9±1.5
Me-4PACz + PTA-COOH	38.94±1.48	37.49±1.09	1.45±0.39	88.78 ±1.71	44.09 ±2.05	16.5±2.5

Table S5. MPPT stability test results (100 mW cm^{-2}, N_2 atmosphere, 50°C) for devices using different HTLs.

Device structure: glass/ITO/NiO_x/HTL/$Cs_{0.05}FA_{0.95}PbI_3$/PEACl/$PC_{61}BM$/BCP/Al

HTL	Aging time, h	V_{OC}, V	J_{SC}, mA cm^{-2}	FF, %	PCE, %
Me-4PACz	0	1.089	25.9	68	19.2
	3	1.075	25.7	67	18.5
	6	1.070	25.7	66	18.1
	9	1.070	25.9	65	18.0
	18	1.053	25.9	62	16.9
	30	1.037	25.9	59	15.8
	60	0.995	25.7	54	13.8
	102	0.948	25.5	48	11.6
	189	0.854	24.1	38	7.8
PTA-COOH	0	1.046	25.6	59	15.8
	3	1.089	25.3	63	17.4
	6	1.094	25.2	65	17.9
	9	1.093	25.3	65	18.0
	18	1.091	25.2	63	17.3
	30	1.093	25.1	62	17.0
	60	1.098	25.1	60	16.5
	102	1.094	25.0	57	15.6
	189	1.088	24.6	52	13.9
Me-4PACz+ PTA-COOH	0	1.114	25.8	72	20.7
	3	1.099	25.7	74	20.9
	6	1.105	25.8	74	21.1
	9	1.105	25.6	74	20.9
	18	1.105	25.6	73	20.7
	30	1.106	25.6	70	19.8
	60	1.104	25.5	67	18.9
	102	1.098	25.6	62	17.4
	189	1.084	25.2	55	15.0

Table S6. Characteristics of flexible p-i-n PSCs (PET/ITO/NiO$_x$/HTL/Cs$_{0.05}$FA$_{0.95}$PbI$_3$/PEACl/ PC$_{61}$BM/BCP/Ag) before and after exposure to gamma rays

HTL	**Dose of gamma rays, kGy**	**Scan direction**	**V$_{OC}$, mV**	***J*$_{SC}$, mA cm^{-2}**	**FF, %**	**PCE, %**
Me-4PACz	0	Forward	1098±7 (1103)*	20.7±0.5 (21.2)	71±3 (73)	16.0±0.8 (17.1)
		Reverse	1102±9 (1106)	20.6±0.5 (21.2)	71±3 (74)	16.1±0.8 (17.4)
	100	Forward	1103±17 (1111)	20.6±0.5 (20.7)	70±5 (72)	15.8±1.3 (16.6)
		Reverse	1105±16 (1107)	20.6±0.5 (20.6)	68±5 (71)	15.4±1.1 (16.2)
PTA-COOH	0	Forward	1083±17 (1114)	20.1±0.4 (20.7)	73±4 (75)	15.9±1.1 (17.3)
		Reverse	1085±18 (1122)	20.1±0.4 (20.6)	73±4 (76)	15.9±1.3 (17.6)
	100	Forward	1040±20 (1036)	19.8±0.3 (20.4)	72±3 (75)	14.7±0.7 (15.9)
		Reverse	1040±30 (1040)	19.8±0.3 (20.4)	71±4 (75)	14.5±0.8 (15.9)
Me-4PACz + PTA-COOH	0	Forward	1105±14 (1112)	20.7±0.4 (21.0)	71±4 (74)	16.1±1.2 (17.3)
		Reverse	1109±18 (1122)	20.6±0.5 (21.0)	71±4 (75)	16.2±1.3 (17.7)
	100	Forward	1109±3 (1113)	20.6±0.2 (20.7)	72±3 (75)	16.5±0.6 (17.3)
		Reverse	1105±10 (1115)	20.6±0.2 (20.7)	70±5 (75)	16.0±1.2 (17.3)

* Average values ± standard deviation are given, while the values in the brackets correspond to the champion cell characteristics

Table S7. Characteristics of flexible p-i-n PSCs (PEN/ITO/NiO_x/Me-4PACz+**PTA-COOH**/ $Cs_{0.05}FA_{0.95}PbI_3$/PEACl/$PC_{61}BM$/BCP/Ag) before and after exposure to different doses of gamma rays (up to 1MGy)

Dose of gamma rays, kGy	**Scan direction**	**V_{OC}, mV**	**J_{SC}, mA cm^{-2}**	**FF, %**	**PCE, %**
0	Forward	1115±7 (1115)*	25.0±0.6 (25.9)	74±3 (76)	21.3±1.1 (22.0)
	Reverse	1118±9 (1122)	24.9±0.6 (25.9)	76±2 (79)	21.6±0.9 (22.9)
100	Forward	1126±12 (1144)	24.6±0.6 (24.5)	72±2 (76)	20.0±0.7 (21.4)
	Reverse	1129±14 (1148)	24.5±0.6 (24.5)	74±2 (78)	20.5±0.9 (21.9)
250	Forward	1111±10 (1125)	23.8±0.4 (24.4)	69±4 (72)	18.4±1.3 (19.7)
	Reverse	1113±11 (1128)	23.7±0.4 (24.3)	70±4 (73)	18.6±1.3 (20.1)
500	Forward	1121±10 (1116)	23.4±0.5 (23.7)	63±3 (68)	16.6±0.8 (17.9)
	Reverse	1121±11 (1119)	23.3±0.5 (23.7)	64±3 (70)	16.7±0.9 (18.5)
1000	Forward	1109±28 (1131)	22.9±0.6 (23.2)	50±5 (54)	12.7±1.3 (14.3)
	Reverse	1107±29 (1129)	22.8±0.6 (23.2)	51±3 (55)	12.8±1.0 (14.4)

* Average values ± standard deviation are given, while the values in the brackets correspond to the champion cell characteristics

Table S8. Characteristics of flexible PSCs using different HTLs extracted from impedance spectroscopy[9] measurements and Mott-Schottky analysis. The impedance spectroscopy measurements were performed in the dark with no bias voltage applied relative to the open-circuit voltage (V_{OC}). Device structure: PEN/ITO/NiO_x/Me-4PACz+**PTA-COOH**/ $Cs_{0.05}FA_{0.95}PbI_3$/PEACl/$PC_{61}BM$/BCP/Ag

Dose, kGy	**R_s, Ω**	**R_{ct}, Ω**	**V_{bi}, V**	**N_{eff}, cm^{-3}**
0	30±3	66±17	0.75±0.08	$7.5 \cdot 10^{13} \pm 1.02 \cdot 10^{13}$
1000	22±3	127±43	0.47±0.19	$1.5 \cdot 10^{14} \pm 1.41 \cdot 10^{13}$

Table S9. Characteristics of flexible PSCs using different HTLs extracted from light-intensity dependence of the short-circuit current density (**α** values) and open-circuit voltage (**n_{id}** values).[10-11] Device structure: PEN/ITO/NiO_x/Me-4PACz+**PTA-COOH**/$Cs_{0.05}FA_{0.95}PbI_3$/PEACl/ $PC_{61}BM$/BCP/Ag

Dose, kGy	**α**	**n_{id}**
0	1.11±0.07	1.24±0.1
1000	1.09±0.03	1.22±0.1

References

[1] C. Gong, H. Li, Z. Xu, Y. Li, H. Wang, Q. Zhuang, A. Wang, Z. Li, Z. Guo, C. Zhang, B. Wang, X. Li & Z. Zang, *Nat. Commun.*, 2024, **15**, 9154

[2] J. Wang, K. Liu, L. Ma and X. Zhan, *Chem. Rev.*, 2016, **116**, 14675–14725.

[3] O. A. Kraevaya, A. F. Latypova, A. A. Sokolova, A. A. Seleznyova, N. A. Emelianov, N. A. Slesarenko, V. Yu. Markov, L. A. Frolova and P. A. Troshin, *Sust. Energy Fuels*, 2022, **6**, 3485–3489.

[4] N. Yaghoobi Nia, M. Méndez, B. Paci, A. Generosi, A. Di Carlo and E. Palomares, *ACS Appl. Energy Mater.*, 2020, **3**, 6853–6859.

[5] Y. Ko, Y. Kim, C. Lee, Y. Kim and Y. Jun, *ACS Appl. Mater. Interfaces*, 2018, **10**, 11633–11641.

[6] E. Mondal, J.-P. Lellouche and M. Naddaka, *ChemistryOpen*, 2015, **4**, 489–496.

[7] S. Tsarev, I. K. Yakushchenko, S. Yu. Luchkin, P. M. Kuznetsov, R. S. Timerbulatov, N. N. Dremova, L. A. Frolova, K. J. Stevenson and P. A. Troshin, *Sust. Energy Fuels*, 2019, **3**, 2627-2632

[8] H. Zhang, X. Qiao, Y. Shen, T. Moehl, S. M. Zakeeruddin, M. Grätzel, and M. Wang, J. *Mater. Chem. A*, 2015, **3**, 11762-11767

[9] X. Luo, J. Ding, J. Wang, J. Zhang, *J. Mater. Res.*, 2020, **35**, 2150–2157

[10] M. Neukom, S. Züfle, S. Jenatsch and B. Ruhstaller, Sci. Technol. *Adv. Mater.*, 2018, **19**, 291–316.

[11] D. Glowienka and Y. Galagan, *Adv. Mater.*, 2022, **34**, 2105920.